Dense granular flow around an immersed cylinder

D. Chehata and R. Zenit[a]

Instituto de Investigaciones en Materiales, Universidad Nacional Autónoma de México,
Apdo. Postal 70-360, Ciudad Universitaria, Coyoacán D.F. 04510, México

C. R. Wassgren

School of Mechanical Engineering, Purdue University, West Lafayette, Indiana 47907-2088

The flow around a fixed cylinder immersed in a uniform granular flow is studied experimentally. Experiments are performed in a tall vertical chute producing a quasi two-dimensional granular flow. A storage bin at the top of the chute feeds glass particles into the channel while the mean velocity of the flow is controlled by varying the exit width of a hopper located at the channel bottom. Measurements of the drag force acting on a fixed cylinder are made using a strain gauge force measurement system. The flow velocity field is measured through a transparent wall using a particle image velocimetry analysis of high speed video recordings of the flow. Experiments are performed for a range of upstream particle velocities, cylinder diameters, and two sizes of glass particles. For the range of velocities studied, the mean drag force acting on the cylinder is independent of the mean flow velocity, contrary to what is expected from any ordinary fluid. The drag force increases with cylinder diameter and decreases with particle diameter. The drag force scales with the asymptotic static stress state in a tall granular bed. The drag coefficient, defined in terms of a dynamic pressure and an effective cylinder diameter, scales with the flow Froude number based on the hydraulic diameter of the channel. This analysis indicates that the drag acting on the cylinder is strongly affected by the surrounding channel geometry. Although the drag force on the cylinder does not change with the upstream flow velocity, the flow streamlines do change with velocity. A large stagnation zone forms at the leading edge of the cylinder while at the trailing edge an empty wake is observed. The wake size increases with flow velocity. Measurements of the flow vorticity and granular temperature are also presented and discussed. © *2003 American Institute of Physics.*
[DOI: 10.1063/1.1571826]

I. INTRODUCTION AND BACKGROUND

Interest in granular material dynamics has increased significantly in recent years. Although many aspects of the governing mechanics of granular flows are now well understood, there are still many areas that have not yet been explored. In particular, the problem of flow around immersed objects still has many unresolved questions.

Fluid flow around immersed objects has been an important subject in the development of modern fluid mechanics. Many phenomena such as drag forces, boundary layers, and the transition to turbulence have advanced with the study of flow around obstacles. This geometry can also be considered a benchmark for investigations of particulate flow mechanics. Such flows are of great importance in many engineering applications and natural phenomena. A recent recount of these can be found in Wassgren *et al.*[1]

Granular flow around obstacles was studied early on by Wieghardt.[2–4] In these studies, partially immersed cylinders were dragged through a static bed of sand to obtain measurements of the drag force. It was found that the drag on the rods had a weak dependence on the translational velocity and the cross-sectional shape of the rods, although there was a square-root dependence on the rods' projected diameters.

Wieghardt reasoned that the weak velocity dependence at slow velocities resulted from sliding friction interactions with the surrounding particles; a mechanism that is independent of velocity. Wieghardt was also able to predict the drag force to within 10% at slow speeds using Coulomb's theory for passive failure in a Mohr-Coulomb material (see, for example, Nedderman[5]).

Recently, Albert *et al.*[6] revisited this experiment with a similar apparatus but using much slower velocities, of the order of 1 mm/s rather than the 1–100 cm/s used by Wieghardt. Albert *et al.* found similar results although a linear dependence on the object's projected diameter was found rather than the square-root dependence observed by Wieghardt.

Note that in both Wieghardt's and Albert *et al.*'s studies the dragged objects were partially immersed in a static granular bed. In such a configuration, the cylinder is subject to a stress field that varies with depth and free surface effects must be considered. Moreover, it was not possible to examine the flow fields around the object.

Schiffer and co-workers[7,8] have recently studied the fluctuating nature of the granular drag. They measured the drag on a partially immersed rod moving slowly in a bed of grains and found that the force-time trace showed a characteristic stepped sawlike fluctuation. The nature of these fluctuations was explained in terms of the formation and rupture of force

---

[a]Author to whom correspondence should be addressed.

chains within the material and the stick-slip behavior of the contacts between grains and the object. In a more recent contribution[9] they have also analyzed the effects of the object's shape on the granular drag and its fluctuations.

Nedderman *et al.*[10] and Tüzün and Nedderman[11,12] studied the flow kinematics and wall stresses around silo inserts. Stagnant zones of material on the upstream side of the inserts were observed in addition to a large void region behind the objects. Recently Amarouchene *et al.*[13] reported on flow patterns around various objects in dilute granular flows. Tsai *et al.*[14] also reported a few sample experiments to demonstrate correlated grain velocities for the case of a flow around an object in a 2-D channel flow. Tai *et al.*[15] reported the formation of shock like structures for the flow of avalanches past obstructions. Similar shock structures have been reported for the case of collisional-dilute granular flows.[1]

Penetration tests are routinely performed by civil engineers to probe the properties of soils. There have been recent attempts to model the flow around penetrometers[16,17] of different geometries, in particular for symmetric cavity configurations, and for different types of soils like clays or sands. In particular, the geometry of the t-bar penetrometer[18] is very similar to that in the present study. Many authors in the soil mechanics community concur it is not yet possible to model accurately the flow of a sandlike material around a t-bar penetrometer.[16,19,20]

The previously discussed studies were performed in dense flow conditions. In a companion paper,[1] we studied a similar problem but for the case of a dilute granular flow. Buchholtz and Pöschel[21] and Zenit and Karion[22] have previously studied the problem in the same regime. These investigations found that the drag force on an object is proportional to the square of the upstream flow velocity, in accordance to what is expected from molecular-gas considerations.

It is well known that the behavior of a granular material changes when particle collision effects, as opposed to frictional effects, dominate the flow.[23] For the case of granular flow around objects, the transition between dense, slow flow and dilute, rapid flow behavior manifests itself as a change in the dependence of the drag force, changing from being velocity independent to velocity-squared dependent. We wish ultimately to investigate the conditions that determine the transition between these two states.

In this paper we present experimental results for the drag force acting on a cylinder immersed in a dense granular flow. With the experimental apparatus used in this study, it is possible to eliminate both the depth dependence and the free surface effects found in the experiments by Wieghardt and Albert *et al.* We present measurements of the drag force on a cylinder for a wide range of velocities and for different cylinder and particle diameters. A good agreement between the present results was found with measurements by Albert *et al.* despite the fact that the experimental conditions were very different. Additionally, we are able to directly observe the flow fields around the cylinder and relate these to the drag force. We also present the flow vorticity and granular temperature fields that, to our knowledge, have not been previously reported. This paper complements our recent study

concerning the drag force on a cylinder in a dilute flow regime.[1]

II. EXPERIMENTAL APPARATUS

A vertical chute was built to generate a quasi two-dimensional flow. A schematic of the experiment is shown in Fig. 1. The channel is 1000 mm tall, $L=300$ mm wide, and the gap width between the front and back glass walls is $W=50$ mm. A storage bin at the top of the chute feeds glass particles into the channel while the mean velocity of the flow is controlled by varying the exit width of a hopper located at the channel exit. To obtain a measurement of the mean flow velocity, the mass flow rate is calculated by measuring the total emptying time of a known mass of particles. Assuming that the initial and final transients are short, the mean upstream grain velocity, U_∞, is calculated as

$$U_\infty = \frac{\dot{m}}{\rho \nu_{max} A},\tag{1}$$

where $\dot{m}$ is the mass flow rate (measured as the total mass divided by the total discharge time), ρ is the particle density, $A=LW$ is the channel cross-sectional area, and ν_{max} is the maximum packing solid fraction. A value of 0.64 for the maximum solid fraction was used. The solid fraction does not remain constant as the particle velocity increases, especially in the vicinity of the cylinder. Hence, the measurement obtained from Eq. (1) is an approximation. This velocity estimate is also corroborated with velocity measurements made using particle image velocimetry (PIV) software. The error involved in considering that the packing remains constant is less than 8% when compared to the measurements obtained by the image processing software.

An aluminum cylinder is positioned at the center of the channel and is held fixed by a pin that passes through the cylinder's axis. The pin also passes through the front and back glass walls without making direct contact with them. One of the pin ends is held fixed while the other is connected to a force transducer. The transducer consists of a calibrated strain gauge array. The voltage from the array is digitized and recorded using a PC-based data acquisition system. Figure 2 shows a force trace obtained from a typical experiment. A residual nonzero force on the cylinder is observed at the beginning of each experiment. This residual force results from filling the channel. When the flow starts (at approximately $t=5$ s in the figure) an initial rapid transient is observed. Since the mass flow rate is independent of the granular head,[5] the measured force reaches a steady mean value about which fluctuations occur. Note that the fluctuations that occur appear to be random. Other investigators[7,8] have observed sawtoothlike fluctuations but for much smaller flow velocities. Near the end of the emptying process, a second transient is observed that corresponds to when there is little material remaining upstream of the cylinder. The measurement of the drag force is performed, for all cases, over the region where the mean drag force is constant.

In addition to the force measurements, the flow is videotaped through the front glass wall of the channel using a high speed videocamera. The images are stored digitally and are
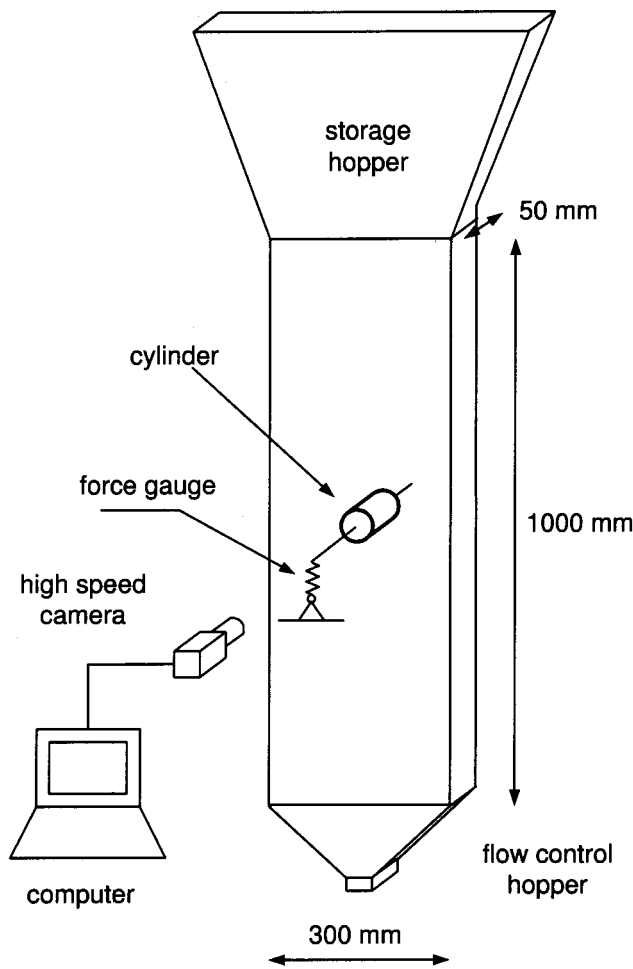
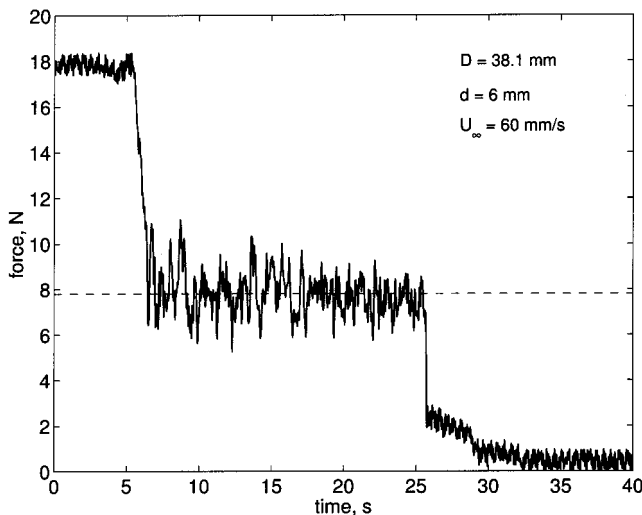FIG. 1. A schematic of the experimental apparatus.

FIG. 2. Force as a function of time for a typical flow. The dashed line shows the value of the mean drag force.
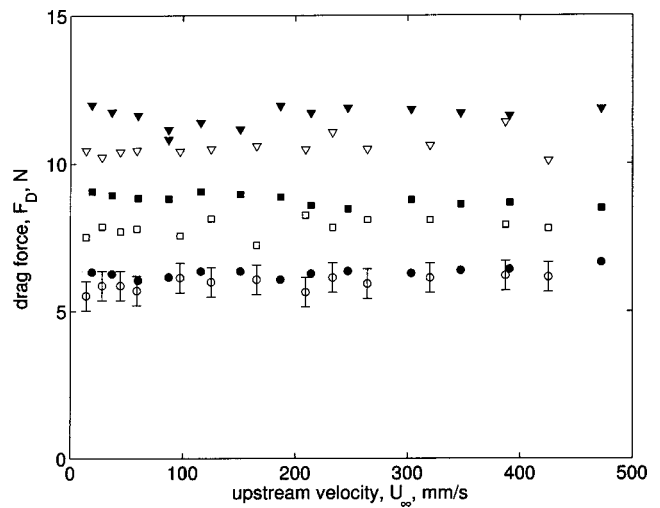

FIG. 3. Force as a function of particle velocity for different particle and cylinder diameters (given in mm). $\bullet$: $D=12.7$, $d=3$; $\blacksquare$: $D=25.4$, $d=3$; $\blacktriangledown$: $D=38.1$, $d=3$; $\bigcirc$: $D=12.7$, $d=6$; $\square$: $D=25.4$, $d=6$; $\triangledown$: $D=38.1$, $d=6$. Scatter bars corresponding to $\pm$ one standard deviation in the force measurements are shown on one of the data sets. Scatter bars for the remaining data sets are left off for clarity.

processed using PIV software to obtain velocity fields around the cylinder. Other quantities of interest, such as the granular temperature and the vorticity, are also calculated.

Many experiments were performed. The drag force and the velocity fields were obtained for a range of upstream particle velocities, U_∞ (from nearly zero to 470 mm/s), for three different cylinder diameters ($D=38.1$ mm, 25.4 mm, and 12.7 mm) and two different sizes of glass particles ($d=6$ mm and 3 mm, $\rho=2500$ kg/m^3). The particles used in all of the experiments were nearly mono-disperse glass spheres (Jayco Co.).

III. RESULTS

A. Drag force and drag coefficient

Measurements of the drag force acting on the cylinder were obtained directly using a strain gauge attached to one of the pinned ends of the cylinder. Figure 3 plots the mean drag force as a function of particle velocity (which varies from nearly zero to approximately 470 mm/s) for three cylinders and two particle diameters. The most striking characteristic of these results is that, for all cases, the drag force is independent of the particle velocity. These results are similar to those reported by Wieghardt[3] and Albert et al.[6] and indicate that the contacts between the cylinder and the particles are of a frictional and enduring nature.

The drag force increases nearly linearly with the cylinder diameter. A secondary, weaker dependence on the particle diameter is also observed where a larger drag force occurs as particle size decreases for a given cylinder size and particle velocity. The linear dependence of the drag force on the cylinder diameter is in agreement with the measurements of Albert et al.[6] but disagrees with Wieghardt[3] who found a square root dependence on the cylinder diameter.

To present the results in dimensionless terms, we use the classical definition of the drag coefficient, C_D,

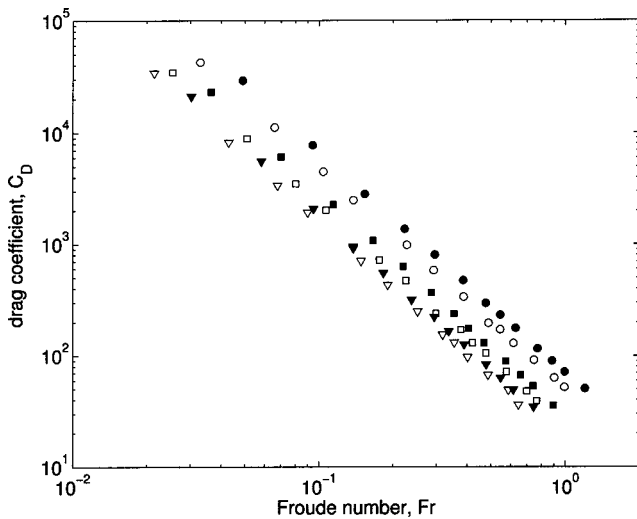$$C_D = \frac{F_D}{\frac{1}{2}\rho \nu_{\max} U_\infty^2 (D+d)(L-d)}, \tag{2}$$

FIG. 4. Drag coefficient as a function of Froude number based on the effective cylinder diameter. The drag coefficient, C_D, is defined in Eq. (2); the Froude number, Fr is defined in Eq. (3). Symbols as in Fig. 3.

FIG. 5. Drag coefficient as a function of the Froude number based on the hydraulic diameter of the channel. The drag coefficient, C_D, is defined in Eq. (2); the Froude number, based on D_H, is defined in Eq. (6). Symbols as in Fig. 3. The additional symbols are the data from Albert *et al.* (Ref. 6) (given in mm): ■: $D=38$, $d=0.41$; ∗, $D=4.7$, $d=3$; ×, $D=19$, $d=3$; +, $D=4.7$, $d=0.88$.

where F_D is the drag force, ρ is the particle mass density, $\nu_{\max}$ is the maximum solid fraction, and $(D+d)(L-d)$ is the effective frontal projected area of the cylinder where L is the length of the cylinder, D is the cylinder diameter, and d is the particle diameter. Figure 4 presents the drag coefficient as a function of the flow's Froude number, Fr, based on the upstream velocity and effective cylinder diameter:

$$\text{Fr}=\frac{U_\infty}{\sqrt{g(D+d)}}. \tag{3}$$

Since the measured drag force is independent of the flow velocity, the drag coefficient decays with the velocity squared. Using the given scaling, however, does not collapse the data very well. It must be noted that by presenting the data in these terms, an artificial U_∞^{-2} dependence is introduced. We present the data in this manner to preserve the classic definition of the drag coefficient intact so that the results can be compared and contrasted with those of ordinary fluids.

To find a more appropriate scaling law, we consider the stress state within a granular material in a vertical bin. The stress in a tall bin is known to asymptote to a constant value that is independent of the depth of the granular head but proportional to the bin's hydraulic diameter, $D_h = 4A_{\text{bin}}/P_{\text{bin}}$ where A_{bin} and P_{bin} are the bin's cross-sectional area and perimeter, respectively.[5] For a vertical channel with a rectangular cross-section, the wall stresses, σ, asymptote to

$$\sigma\propto\rho\nu g D_h=\rho\nu g\,\frac{2(L-d)(W-d)}{(L+W-2d)}, \tag{4}$$

where $(L-d)(W-d)$ and $2(L+W-2d)$ are the effective cross-sectional area and perimeter of the channel (including finite particle size effects), respectively, L and W are the length and width of the channel respectively, and g is the acceleration due to gravity. Neglecting the variations of the
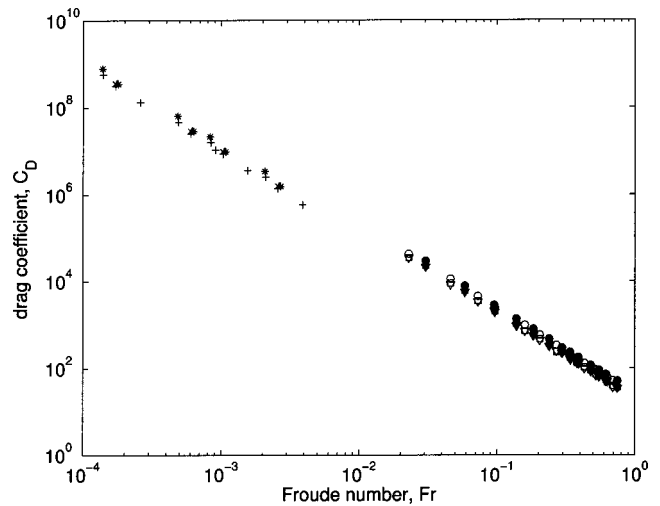
solid fraction, ν, around the cylinder and assuming that the stress acts equally around the entire surface of the cylinder, the drag force is of the form

$$F_D\propto D_h(D+d)(L-d)$$
$$=\frac{2(L-d)(W-d)}{(L+W-2d)}(D+d)(L-d). \tag{5}$$

To represent the measured drag forces in terms of this scaling, and keeping the classical definition of the drag coefficient intact [Eq. (2)], we define a Froude number based on the hydraulic diameter of the channel, D_h:

$$\text{Fr}=\frac{U_\infty}{\sqrt{gD_h}}=\frac{U_\infty\sqrt{(L+W-2d)}}{\sqrt{2g(L-d)(W-d)}}. \tag{6}$$

Figure 5 plots the drag coefficient as a function of the Froude number defined using Eq. (6). Compared to the previous Froude number scaling shown in Fig. 4, the Froude number scaling using a hydraulic diameter does a better job of collapsing the data. It is interesting to note that this scaling of the drag force was obtained by considering a static stress state in a tall granular bin. It can be argued that despite the fact that the material is flowing, the static stress distribution remains unchanged. It will be seen in the next section, however, that the flow field does change significantly with the flow velocity; a seemingly contradictory observation when considering the independence of the drag force on the flow velocity.

Note that for the case when $L\ll W$, Eq. (5) can be simplified using the binomial expansion theorem,

$$F_D\propto(L-d)^2(D+d)\left(1-\frac{L-d}{W-d}+\left(\frac{L-d}{W-d}\right)^2-\cdots\right). \tag{7}$$

Hence, when $L\ll W$, the drag force is directly proportional to the effective diameter of the cylinder, $D+d$, and the square of its effective length, $L-d$.
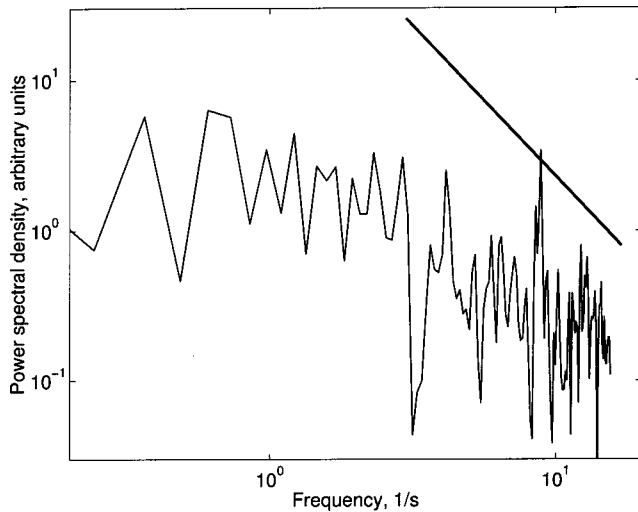
FIG. 6. Power spectrum of the force fluctuations as a function of frequency for a typical flow (data from Fig. 2). The solid line shows an f^{-2} decay.

FIG. 7. Standard deviation of the force as a function of particle velocity for different particle and cylinder diameters. Symbols as in Fig. 3.

Along with the scaled measurements, the data from Albert *et al.*[6] are presented, scaled according to Eqs. (2) and (6). To calculate the corresponding hydraulic diameter for Albert's data set, we considered W to be the radius of the container and L the bar immersion depth. The scaling works remarkably well. The data collapses onto the same line for the present experiments but for a much smaller range of Froude numbers. There is a slight shift between the best fit line of the two experimental data sets, which may result from differences in particle-cylinder surface roughness for the two experiments.

B. Drag force fluctuations

Figure 2 shows a typical force trace obtained from the experiment. Clearly, there is a characteristic fluctuation in the force as the material flows around the cylinder. Previous studies of fluctuations in the granular drag have revealed information about the dynamics of the particle contacts, formation of force chains, and many other rich phenomena.[6,8] Figure 6 shows the power spectrum of the force fluctuations (arbitrary units), from the data shown in Fig. 2, as a function of the frequency. The force fluctuations occur over a wide range of frequencies. The spectra shows a decay slightly smaller than the typical f^{-2}, which has been reported to be associated with stick-slip phenomena in granular flows.[8]

The mean force fluctuation was calculated for all the experiments. Figure 7 shows the standard deviation of the drag force for the cases shown in Fig. 3 as a function of the mean upstream grain velocity. The fluctuation of the drag force increases monotonically with velocity despite the fact that the mean drag is independent of the grain velocity. As the flow velocity increases, the formation and destruction of force chains, responsible of the drag force fluctuations, occurs at a higher rate. Hence, it is expected that the fluctuations would increase with velocity. Note also that the force fluctuations do not approach a zero value for small velocities. For a given grain velocity, the fluctuations increase with
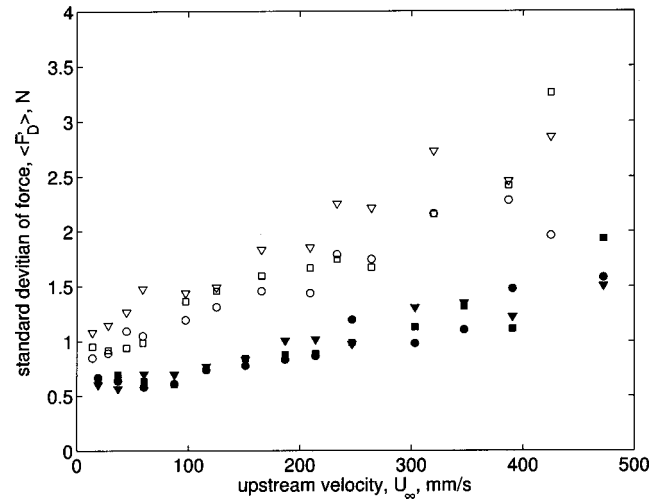
the cylinder diameter and appear to increase slightly with particle diameter.

C. Visualization and flow fields

A photograph of a typical flow is shown in Fig. 8. The camera shutter remained open for a fraction of a second so that moving particles traced flow streamlines. The velocity is nearly uniform upstream from the cylinder (as will be dis-
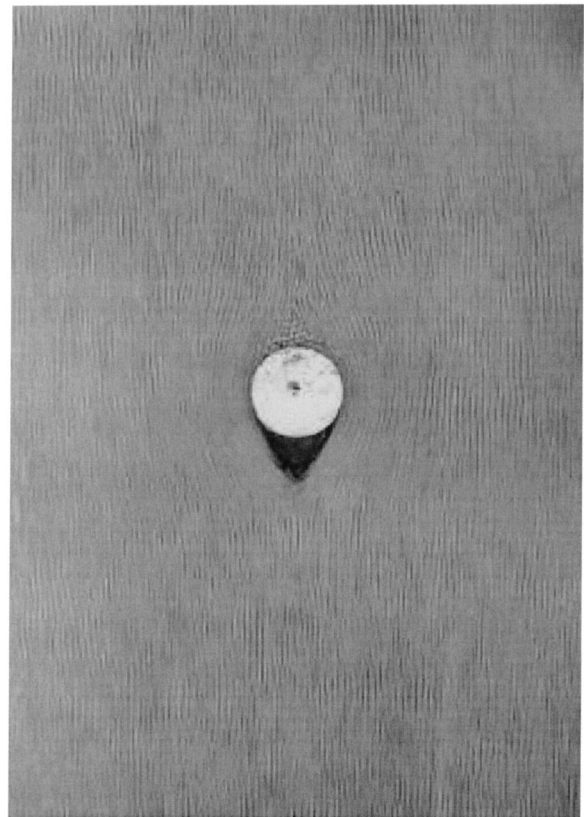

FIG. 8. Photograph of a typical flow. The camera shutter remained open for a fraction of a second so that the flow streamlines were traced by the moving particles. $U_\infty = 470$ mm/s, $d = 3$ mm, and $D = 38.1$ mm.
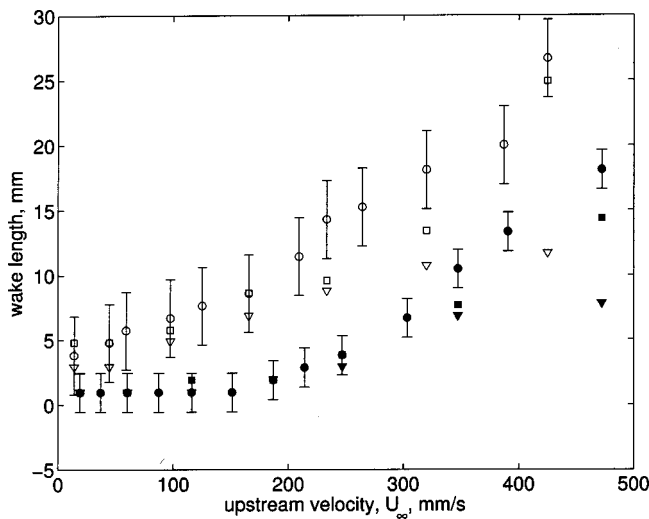
FIG. 9. Wake length as a function of upstream flow velocity. Measurement error bars corresponding to $\pm\frac{1}{2}d$ are shown on two of the data sets. Error bars for the remaining data sets are left off for clarity. Symbols as in Fig. 3.

FIG. 10. Dimensionless wake length as a function of Froude number based on the effective cylinder diameter. Symbols as in Fig. 3.

cussed in Sec. III C 1). A stagnation region forms on the upstream side of the cylinder while an empty wake occurs downstream of the cylinder. The appearance of the wake may result from a combination of two effects. First, tensile stresses may exist at the cylinder's trailing edge and since the cohesionless glass spheres cannot sustain tensile loads, an empty wake forms. Second, the wake may result because the flow's granular temperature at the cylinder's trailing edge is too small to overcome the particles' inertia. Hence, particles cannot move into the empty wake region. The size and shape of the stagnation region remains approximately constant over the range of flow velocities examined, but the size of the wake increases monotonically with particle velocity. Tsai et al.[14] also observed an empty wake behind a cylinder immersed in a two-dimensional granular flow. They observed of zones in which the fluctuating velocity had similar values termed "velocity correlation zones." They explained the appearance of the wake in terms of these correlation zones. However, they showed just one result for a particular condition; a more in depth analysis was not performed. Hence, an explanation of our measurements cannot be formulated in these terms.

The length of the wake was obtained by directly measuring the distance between the trailing edge of the cylinder and the position at which the wake closed. Figure 9 plots the wake length, λ, as a function of the flow velocity, U_∞, for various cylinder and particle diameters. Assuming that the wake length is a function of the upstream velocity, gravity, and particle and cylinder diameters, the Buckingham-Pi theorem states that the dimensionless wake length will depend on two other dimensionless parameters. Figure 10 plots the wake length normalized by the effective cylinder diameter, $\lambda/(D+d)$, as a function of the dimensionless particle velocity expressed in terms of the Froude number defined in Eq. (3). Plotting the data in terms of these parameters collapses the data to two curves with the wake length increasing monotonically with Froude number. The wake is slightly larger for larger particles at a given value of the Froude
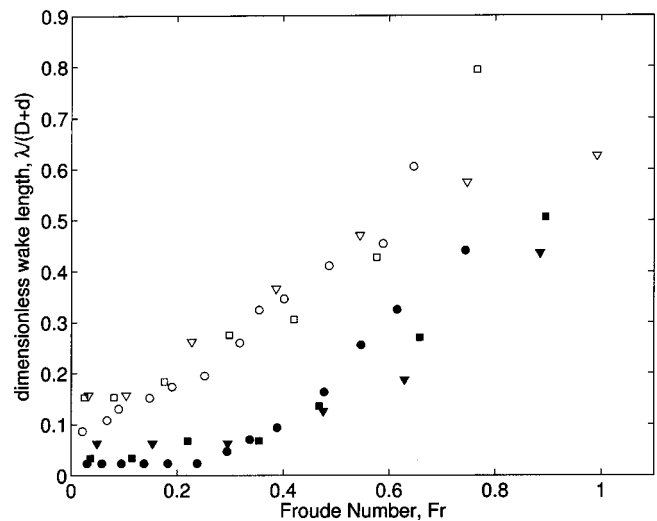
number, presumably due to the effect of increased inertial forces.

Although inertial forces are more significant as the flow velocity increases, the drag force remains independent of the mean flow velocity. Therefore, the drag force on the cylinder appears to be determined solely by the compressive stresses acting on the leading edge of the object where the stagnation zone forms. Since a large void region occurs at the trailing edge of the cylinder, the force contribution from the rear edge of the cylinder is zero. Furthermore, the drag independence on the velocity suggests that the stresses acting on the stagnation zone are very similar to the static stresses in a tall granular bed.

1. Flow velocity fields

The velocity field around the cylinder was obtained by digitally processing the flow images from a high speed video camera using PIV software. Pairs of images are cross-correlated to obtain displacement fields that are then used to obtain the velocity fields for a known frame rate.[24] For all cases, at least 100 pairs of images are averaged to obtain the velocity fields. The processed images are those corresponding to the constant mean drag force time interval. Figure 11 shows an image of a typical flow onto which its corresponding velocity vector map has been overlaid. The velocity profile upstream of the cylinder is uniform. The particle velocity decreases gradually along the channel centerline to form a large stagnation zone at the cylinder's leading edge. The changes in the particle velocity are observed more clearly in Fig. 12(a) which presents the velocity field in terms of the particle speed defined as

$$|\mathbf{u}| = \sqrt{u_x^2 + u_y^2}, \tag{8}$$

where u_x and u_y are, respectively, the horizontal and vertical components of particle velocity, $\mathbf{u}$. Additionally, line plots of the crosswise change of the particle speed for fixed streamwise positions are shown in Fig. 12(b). The numbered vertical lines in Fig. 12(a) depict the different stream wise positions at which the line plots are shown.
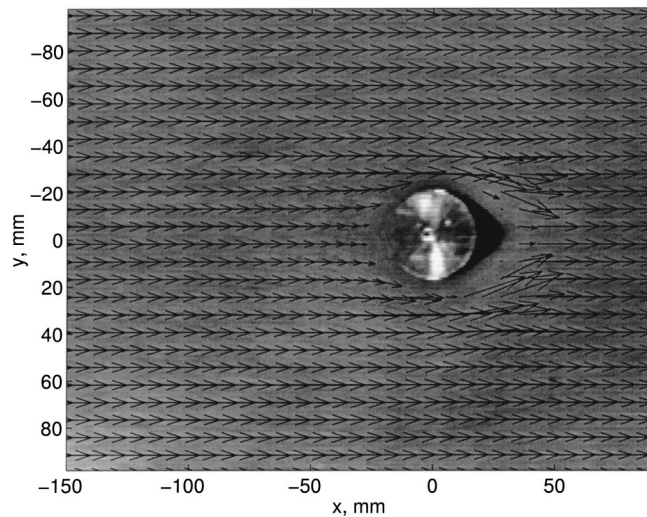
FIG. 11. Flow image with its corresponding vector map. $U_\infty = 336$ mm/s, $D = 38.1$ mm, $d = 3$ mm.
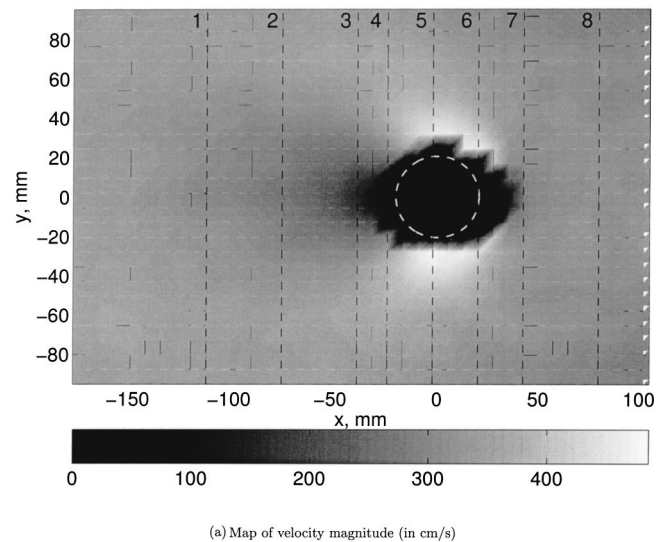

(a) Map of velocity magnitude (in cm/s)

(b) Cross-stream variation of velocity magnitude (in cm/s)

FIG. 12. Velocity magnitude field. The vertical lines in (a) depict the streamwise positions at which the cross-stream variation of the particle speed is shown in (b): line (1), $x/D = -3.0$; line (2), $x/D = -2.0$; line (3), $x/D = -1.0$; line (4), $x/D = -0.6$; line (5), $x/D = 0.0$; line (6), $x/D = 0.5$; line (7), $x/D = 1.1$; line (8), $x/D = 2.1$. Flow parameters as in Fig. 11.

The velocity increases as the particles move around the cylinder. The velocity on either side of the cylinder is significantly larger, up to 40% larger, than the upstream velocity. This increase could be explained, in part, from mass conservation: the obstruction caused by the cylinder causes an increase in the flow around it (assuming an incompressible flow); however, the velocity increase is only observed in the vicinity of the cylinder. The local velocity increases around the sides of the cylinder indicates that the flow slips in these regions since, if the flow behaved in a viscous manner, the flow disturbance would manifest itself as a decay in the speed near the surface of the stationary cylinder.

Fore-aft asymmetry in the velocity field is not observed in the vicinity of the cylinder; however, the velocity profile recovers its uniform distribution within a cylinder diameter downstream of the object. Note that the irregularities observed in the flow field near the surface of the cylinder result from the finite size of the velocity measurement grid. The grid size was approximately 2.5×2.5 and 5×5 particle diameters for the 6 and 3 mm particles, respectively.
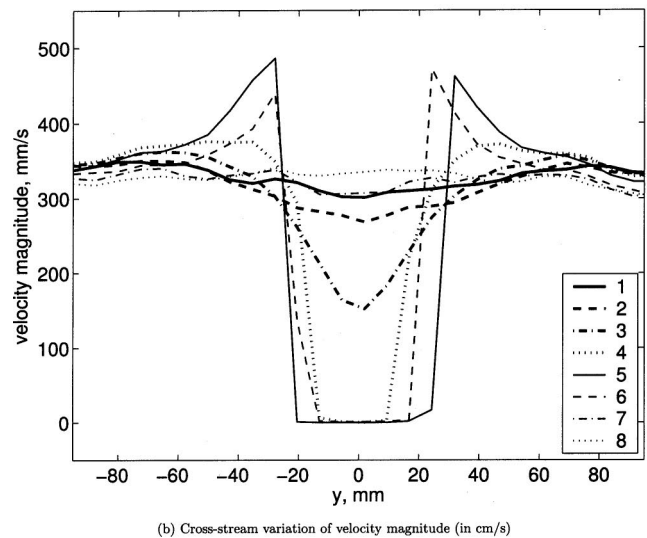
Figures 13(a), 14(a), and 15(a) show line plots of the speed for different flow parameters. To make direct comparisons between different cases, these plots are presented in dimensionless terms. The dimensionless particle speed is defined as

$$\hat{u} = \frac{|\mathbf{u}|}{U_\infty}, \tag{9}$$

where U_∞ is the mean particle velocity upstream of the cylinder [defined in Eq. (1)]. The vertical and horizontal distances are made dimensionless using the cylinder diameter, $\hat{x} = x/D$ and $\hat{y} = y/D$. The figures indicate that the velocity fields are similar for most cases when presented in terms of these dimensionless quantities. Some differences can be observed for the case of the smallest cylinder, $D = 12.7$ mm and for the large particles, $d = 6$ mm.

2. Vorticity field

In the previous section it was noted that the flow appears to slip around the cylinder. It is, therefore, of interest to calculate the flow vorticity and to compare it, in a qualitative manner, to the ideal fluid flow case. The vorticity, ω, is defined as the curl of the velocity field:

$$\omega = \nabla \times \mathbf{u}. \tag{10}$$

In the present, two-dimensional flow, only the component perpendicular to the flow, ω_z, is nonzero. Figure 16 shows the vorticity field and vorticity line plots of the typical flow shown in Fig. 11. The flow is nearly irrotational upstream and downstream of the cylinder. A narrow region of nonzero vorticity appears in the vicinity of the cylinder. Hence, the rotation of regions of particles is only important near the cylinder. It is interesting to note that the vorticity created by the cylinder-flow interaction remains confined to a small re-

(a) Dimensionless velocity
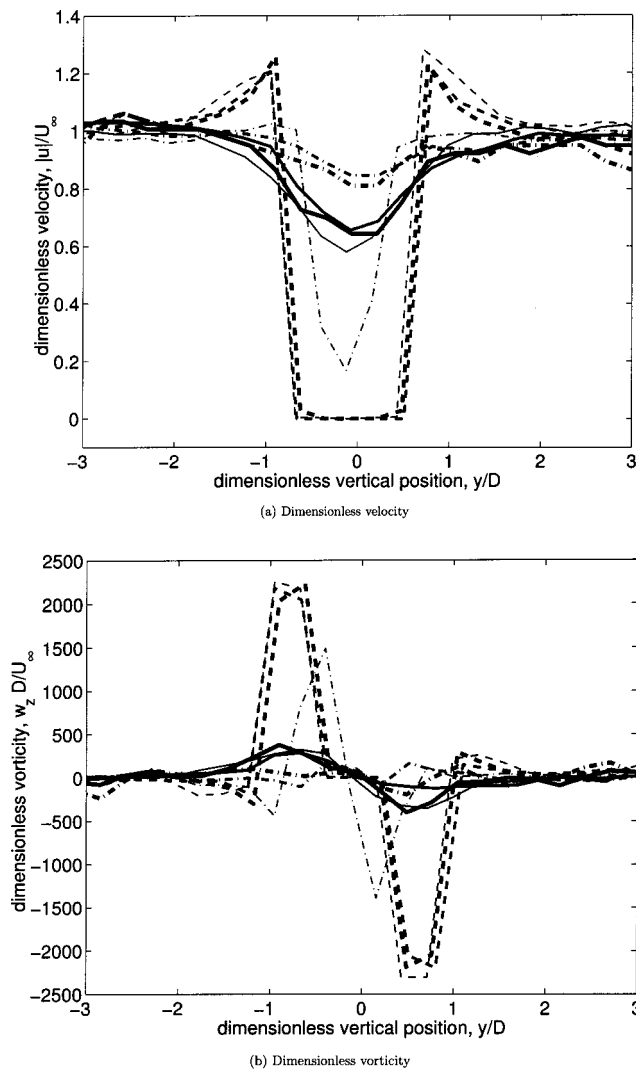

(b) Dimensionless vorticity

FIG. 13. Cross-stream variation of dimensionless particle speed and dimensionless vorticity for different upstream velocities, for a fixed cylinder and particle diameter ($D = 25.4$ mm, $d = 3$ mm). The different line types show different streamwise positions: continuous line (—), $x/D \approx -1.1$; dashed line (- - -), $x/D \approx 0.0$; dashed-dotted line (- · -), $x/D \approx +1.1$. The thin lines correspond to $U_\infty = 345$ mm/s, the medium thick lines correspond to $U_\infty = 131$ mm/s; the thick lines correspond to $U_\infty = 36$ mm/s.

(a) Dimensionless velocity line plot
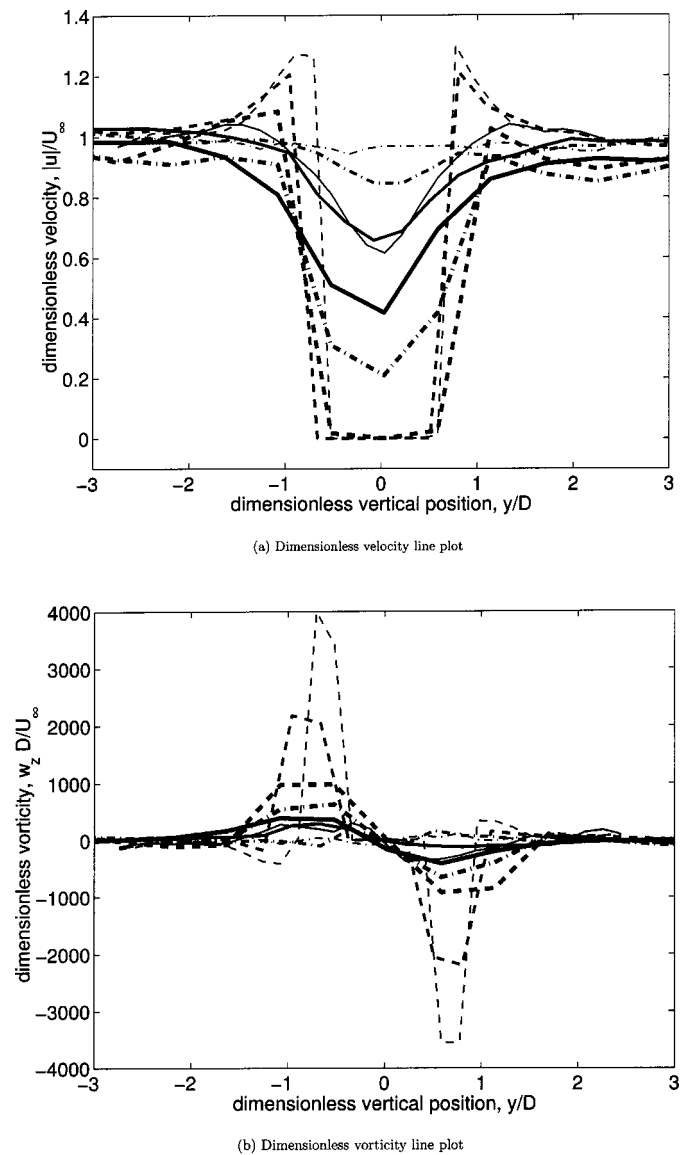

(b) Dimensionless vorticity line plot

FIG. 14. Cross-stream variation of dimensionless particle speed and dimensionless vorticity for different cylinder diameters, for an approximately fixed particle speed and fixed particle diameter ($d = 3$ mm). The different line types show the same stream-wise positions as in Fig. 13. The thin lines correspond to $U_\infty = 113$ mm/s, $D = 38.1$ mm; the medium thick lines correspond to $U_\infty = 131$ mm/s, $D = 25.3$ mm; the thick lines correspond to $U_\infty = 120$ mm/s, $D = 12.7$ mm.

gion near the cylinder and is not diffused nor convected to the rest of the flow domain. Also, the vorticity field appears to be approximately fore-aft symmetric with respect to the cylinder despite the fact that the velocity field is asymmetric.

To compare the vorticity fields for different experiments, we define the dimensionless vorticity as

$$\widehat{\omega_z} = \frac{\omega_z D}{U_\infty}. \tag{11}$$

Figures 13(b), 14(b), and 15(b) show dimensionless vorticity line plots for different flow parameters. For all cases, the flow vorticity remains confined to a region near the sides of the cylinder. The dimensionless magnitude of the vorticity field appears to increase as the cylinder diameter decreases but appears to be independent of the flow velocity and the particle diameter. Also, the zone of nonzero vorticity becomes thinner as the cylinder diameter decreases.

3. Granular temperature field

Another quantity of interest in the study of granular materials is the granular temperature, T, defined as

$$T = \tfrac{1}{2}(\langle u_x' \rangle^2 + \langle u_y' \rangle^2), \tag{12}$$

where $\langle u_x' \rangle$ and $\langle u_y' \rangle$ are the horizontal and vertical particle velocity fluctuations, respectively. The granular temperature, or variance of the particle velocity, is calculated by measuring the mean square deviation of the velocity with respect to the *local mean* for each spatial point. The granular temperature is a measure of the fluctuating kinetic energy of the flow. Figure 17 shows the calculated granular temperature of the flow field shown in Fig. 11. The granular temperature has nonzero values only in the vicinity of the cylinder indicating that it is the interaction with the cylinder that creates the

(a) Dimensionless velocity line plot
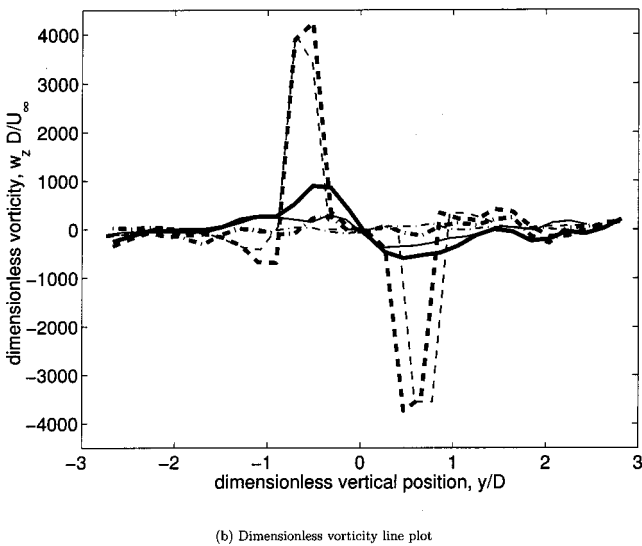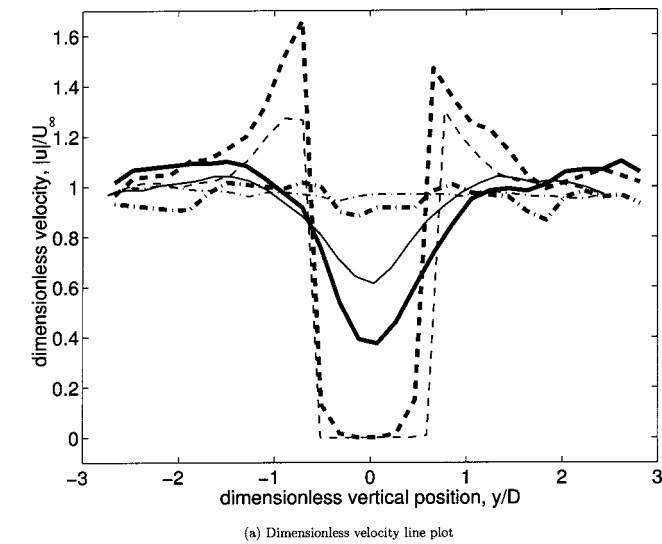

(b) Dimensionless vorticity line plot

FIG. 15. Cross-stream variation of dimensionless particle speed and dimensionless vorticity for different particle diameters, for an approximately fixed particle speed and fixed cylinder diameter ($D = 38.1$ mm). The different line types show the same stream-wise positions as in Fig. 13. The thin lines correspond to $U_\infty = 120$ mm/s, $d = 6$ mm; the thick lines correspond to $U_\infty = 113$ mm/s, $d = 3$ mm.

(a) Vorticity (in 1/s)

(b) Cross-stream variation of vorticity (in 1/s)

FIG. 16. Vorticity field. The line plots in (b) are for the same positions as in Fig. 12. Flow parameters as in Fig. 11.

source of particle velocity fluctuations. In particular, the "hot" spots occur primarily in the vicinity of the wake where a free surface exists. The granular temperature damps out immediately after the particles move away from the cylinder. Temperature fields for the different flow conditions were also obtained and similar characteristics were found for all cases.

IV. CONCLUSIONS

We have obtained direct measurements of the drag force on a cylinder immersed in a granular flow. The experimental apparatus eliminates the bed depth dependence and free surface effects found in previous drag studies.[3,6] Direct measurements of the velocity field around the cylinder were also made by digitally processing high speed video images of the flow.
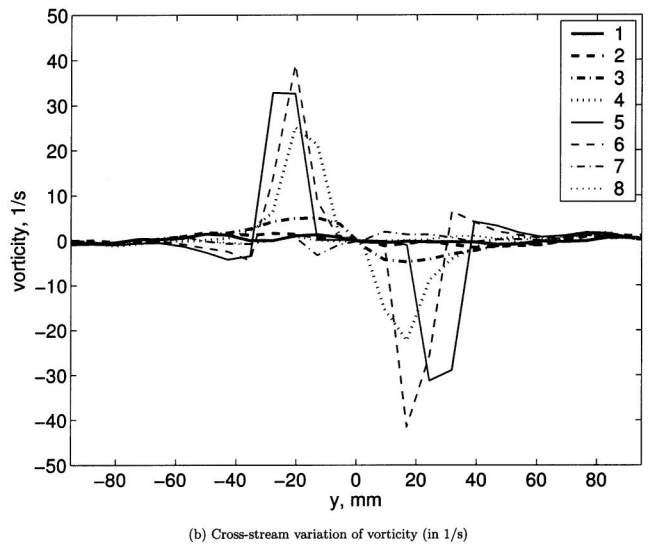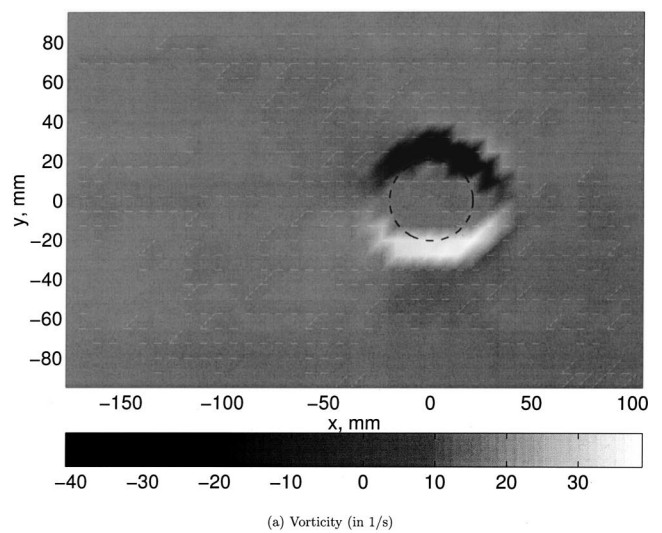
The granular drag force was found to be independent of the mean, upstream particle velocity. This is an indication that frictional drag forces are dominant over inertial effects. The drag force depends strongly on the cylinder diameter with a secondary, weaker dependence on the surrounding particle diameter. Expressed in dimensionless terms, the drag coefficient for the cylinder [Eq. (2)] varies inversely with the square of the flow Froude number based on the hydraulic diameter of the channel [Eq. (6)]. This study indicates that the measured drag force is strongly influenced by the containing walls of the channel. We may expect that the drag force would be different if the experiments were performed in a very wide channel where the granular stresses behaved hydrostatically ($\sigma \propto \rho \nu g$). We found that the present drag measurements agree well with other studies when presented in terms of the drag coefficient and the Froude number based on the hydraulic diameter of the flow.

Flow visualization and velocimetry show that a large stagnation zone forms on the upstream side of the cylinder with particles accelerating as they move around the surface

Phys. Fluids, Vol. 15, No. 6, June 2003

Dense granular flow around an immersed cylinder   1631

(a) Granular temperature (in cm²/s²).

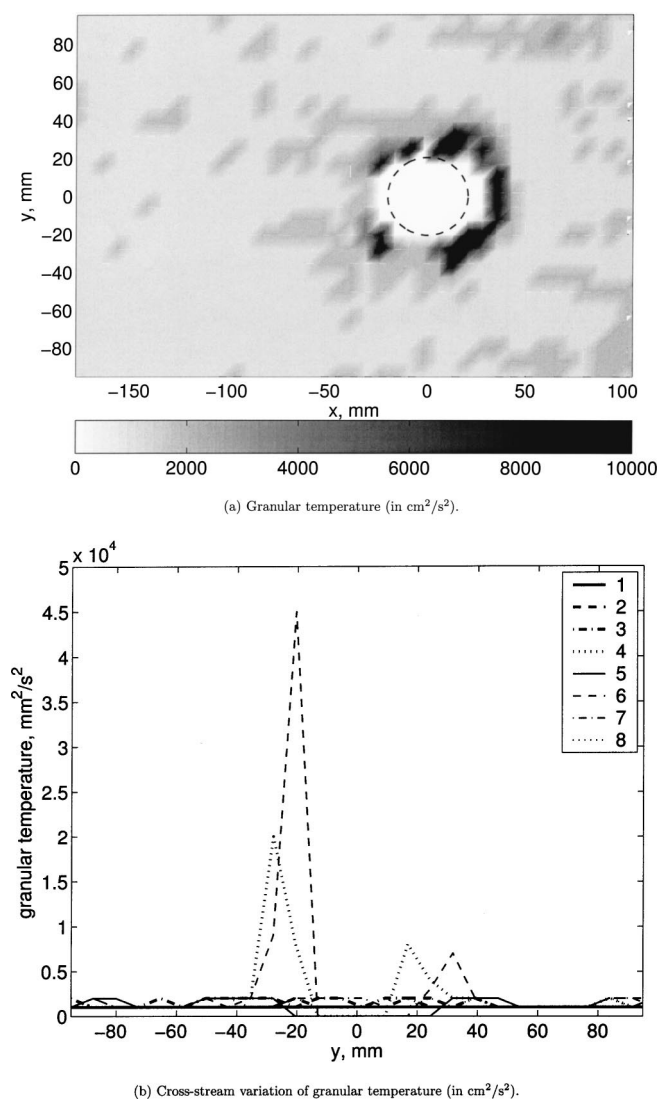(b) Cross-stream variation of granular temperature (in cm²/s²).

FIG. 17. Granular temperature field. The line plots in (b) are for the same positions as in Fig. 12. Flow parameters as in Fig. 11.

of the cylinder. An empty wake forms on the downstream side of the cylinder and grows with the mean flow velocity. Since the downstream flow around the cylinder changes with mean particle velocity but the drag force remains unchanged, the granular drag must result from the compressive stresses acting on the upstream stagnation region. The vorticity and granular temperature of the flow have significant magnitudes only in the vicinity of the cylinder.

A more in depth analysis of the velocity profiles in the vicinity of the cylinder is needed to determine the extent of the stagnation zone and its transition to flow. Measurements of the stress field around the cylinder are required to confirm the hypothesis that the granular drag is dominated by the compressive stresses acting on the stagnation zone. It would also be of interest to increase the range of particle velocities since, for larger velocities, inertial effects are expected to become more significant. The transition from a purely frictional drag force to a frictional/inertial drag force has not yet been identified.

[1]C. R. Wassgren, R. Zenit, and A. Karion, "Dilute granular flow around an immersed cylinder," Proceedings of the Fourth World Congress on Particle Technology, Sydney, Australia (2002) [also submitted to Phys. Fluids].
[2]K. Wieghardt, "Über einige Versuche an Strömungen in Sand," Ing. Arch. **20**, 109 (1952).
[3]K. Wieghardt, "Forces in granular flow," Mech. Res. Commun. **1**, 3 (1974).
[4]K. Wieghardt, "Experiments in granular flow," Annu. Rev. Fluid Mech. **7**, 89 (1975).
[5]R. M. Nedderman, *Statics and Kinematics of Granular Materials* (Cambridge University Press, Cambridge, 1992).
[6]R. Albert, M. A. Pfeifer, A.-L. Barabási, and P. Schiffer, "Slow drag in a granular medium," Phys. Rev. Lett. **82**, 205 (1999).
[7]I. Albert, P. Tegzes, R. Albert, J. G. Sample, M. A. Pfeifer, A.-L. Barabási, T. Vicsek, and P. Schiffer, "Jamming and fluctuations in granular drag," Phys. Rev. Lett. **84**, 5122 (2000).
[8]I. Albert, P. Tegzes, R. Albert, J. G. Sample, A.-L. Barabási, T. Vicsek, B. Kahng, and P. Schiffer, "Stick-slip fluctuations in granular drag," Phys. Rev. E **64**, 031307 (2001).
[9]I. Albert, J. G. Sample, A. J. Morss, S. Rajagopalan, A.-L. Barabási, and P. Schiffer, "Granular drag on a discrete object: Shape fluctuations and jamming," Phys. Rev. E **64**, 061303 (2001).
[10]R. M. Nedderman, S. T. Davies, and D. J. Horton, "The flow of granular materials round obstacles," Powder Technol. **25**, 215 (1980).
[11]U. Tüzün and R. M. Nedderman, "Gravity flow of granular materials round obstacles—I: Investigation of the effects of inserts on flow patterns inside a silo," Chem. Eng. Sci. **40**, 325 (1985).
[12]U. Tüzün and R. M. Nedderman, "Gravity flow of granular materials round obstacles—II. Velocity distributions in slow flow," Chem. Eng. Sci. **40**, 337 (1985).
[13]Y. Amarouchene, J. F. Boudet, and H. Kellay, "Dynamic sand dunes," Phys. Rev. Lett. **86**, 4286 (2001).
[14]J.-C. Tsai, W. Losert, G. A. Voth, and J. P. Gollub, "Two-dimensional granular Poiseuille flow on an incline: Multiple dynamical regimes," Phys. Rev. E **65**, 011306 (2002).
[15]Y. C. Tai, J. M. N. T. Gray, K. Hutter, and S. Noelle, "Flow of dense avalanches past obstructions," Ann. Glaciol. **32**, 281 (2001).
[16]R. Salgado, J. K. Mitchell, and M. Jamiolkowski, "Cavity expansion and penetration resistance in sand," J. Geotech. Geoenviron. Eng. **123**, 344 (1997).
[17]D. P. Randolph, C. M. Martin, and Y. Hu, "Limiting resistance of a spherical penetrometer in cohesive material," Geotechnique **50**, 573 (2000).
[18]D. P. Steward and M. F. Randolph, "T-bar penetration in soft clay," Research Report No. G:1122, The University of Western Australia (1994).
[19]I. Herle and G. Gudehus, "Determination of parameters of a hypoplastic constitutive model from properties of grain assemblies," Mech. Cohesive-Frict. Mater. **4**, 461 (1999).
[20]J. M. Hill, "Some symmetrical cavity problems for a hypoplastic granular material," Q. J. Mech. Appl. Math. **53**, 111 (2000).
[21]V. Buchholtz and T. Pöschel, "Interaction of a granular stream with an obstacle," Granular Matter **1**, 33 (1998).
[22]R. Zenit and A. Karion, "Granular flow around a cylinder," Proceedings of the 2000 AIChE Annual Fall Meeting (2000).
[23]C. S. Campbell, "Rapid granular flows," Annu. Rev. Fluid Mech. **22**, 57 (1990).
[24]R. J. Adrian, "Particle-imaging techniques for experimental fluid-mechanics," Annu. Rev. Fluid Mech. **23**, 261 (1991).